# Analysis of Electron Injection in Laser Wakefield Acceleration Using Betatron Emission in Capillary Tubes

F. G. Desforges[a], B. S. Paradkar[a], M. Hansson[b], T. L. Audet[a], J. Ju[a], I. Gallardo-González[b],
B. Aurand[b], P. Lee[a], L. Senje[b], A. Persson[b], S. Dobosz Dufrénoy[c], O. Lundh[b], G. Maynard[a],
P. Monot[c], J. L. Vay[d], C.-G. Wahlström[b] and B. Cros[a]

[a]Laboratoire de Physique des Gaz et des Plasmas, CNRS-Université Paris-Sud , 91405, Orsay, France
[b]Department of Physics, Lund University, P.O. Box 118, S-22100 Lund, Sweden
[c]Laboratoire Interactions, Dynamique et Lasers, CEA Saclay, 91191 Gif-sur-Yvette, France
[d]Lawrence Berkeley National Laboratory, Berkeley, California 94720, USA

## ABSTRACT

The dynamics of ionization-induced electron injection in the high density ($\sim 1.2 \times 10^{19}\text{cm}^{-3}$) regime of Laser Wakefield Acceleration (LWFA) was investigated by analyzing betatron X-ray emission inside dielectric capillary tubes. A comparative study of the electron and betatron X-ray properties was performed for both self-injection and ionization-induced injection. Direct experimental evidence of early onset of ionization-induced injection into the plasma wave was obtained by mapping the X-ray emission zone inside the plasma. Particle-In-Cell (PIC) simulations showed that the early onset of ionization-induced injection, due to its lower trapping threshold, suppresses self-injection of electrons. An increase of X-ray fluence by at least a factor of two was observed in the case of ionization-induced injection due to an increased trapped charge compared to self-injection mechanism.

**Keywords:** Laser-wakefield acceleration, betatron radiation, self-injection, ionization-induced injection

## 1. INTRODUCTION

Since the theoretical prediction[1] of electron acceleration in a plasma wave driven by a laser pulse, evidence of large amplitude electric field (100 GV/m) and subsequent electron acceleration to MeV energies have been reported from numerous experiments[2–4] . More recently[5–7] , production of quasi-monoenergetic GeV electrons have been demonstrated in the bubble regime[8] , where an ion cavity is formed by the near-total expulsion of electrons initially located in the path of the laser. For adequate laser-plasma parameters[9] , self-injection may occur: electrons from the background plasma are injected into the bubble, then accelerated to relativistic energies. During their acceleration, electrons are subjected to the radial focusing force existing inside the cavity[10] which leads to a transverse oscillatory betatron motion, and so emission of radiation in the X-ray domain. Electron acceleration in the bubble regime is a very promising technique aiming at various applications, such as the development of the next generation of compact X-ray sources with femtosecond pulse duration and micron source size. Typically, current experiments[11–15] are able to produce up to $\sim 10^9$ photons per pulse with peak spectral brightness in the range of $10^{20} - 10^{22}$ photons/(s mm$^2$mrad$^2$0.1%BW) using 50 - 100 TW laser systems.

For a successful realization of a practical LWFA based X-ray source, it is crucial to improve the efficiency of X-ray generation. Since X-ray fluence is proportional to charge[15] , increasing the amount of trapped and accelerated electrons for constant laser parameters would be a significant step toward an efficient compact femtosecond X-ray source. This can be achieved in two ways:

---

Send correspondence to:
F. G. Desforges .: E-mail: frederic.desforges@u-psud.fr, Telephone: +33 (0)1 69 15 81 76
or,
B. Cros: E-mail: brigitte.cros@u-psud.fr, Telephone: +33 (0)1 69 15 81 77

1. The trapped charge is maximum when the LFWA is operated near the beam loading limit, where the amplitudes of the laser wakefield and the electron bunch wakefield are comparable. For the laser pulses commonly used in LWFA experiments, beam loading occurs in the high density operation regime: $n_{e0} \sim 10^{19}\,\mathrm{cm}^{-3}$.

2. The ionization-induced injection mechanism[16–20] offers an attractive alternative to the self-injection mechanism for the optimization of X-ray generation. In this mechanism, inner shell electrons of high atomic number gas are ionized near the laser peak intensity, and preferentially trapped in the plasma wave. The electron injection starts for lower laser intensity compared to self-injection, resulting in an earlier time of injection onset. This increases the time during which electrons radiate, and leads to a higher X-ray fluence.

We report here a comparative study of electron and X-ray properties for both self-injection and ionization-induced injection mechanisms in the high density regime near beam-loading threshold. By analyzing betatron radiation, we give an experimental demonstration of the early onset of the ionization-induced injection due its lower injection threshold compared to self-injection. This result is obtained by using a technique similar to pinhole imaging of the betatron radiation inside a long dielectric capillary tube[15, 21, 22] . Previous experiments[16–19] have demonstrated ionization-induced injection by operating below the self-injection threshold. With the help of numerical simulations, we demonstrate that this early ionization-induced injection of electrons in the ion cavity suppresses subsequent self-injection. We also report a significant increase, by at least a factor of two, of the X-ray fluence when ionization-induced injection is used compared to self-injection. The improvement of the X-ray yield is pre-dominantly due to an increase of trapped charge. The remaining part of this paper is organized as follows: the experimental arrangement is described in Sec. 2, while the results on accelerated electrons and emitted X-rays are presented in Sec. 3. PIC simulations using the WARP code were performed, their results are reported and used to discuss experimental results in Sec. 4.

## 2. EXPERIMENTAL SETUP

### 2.1 Laser Beam

Experiments were performed at the Lund Laser Centre (LLC) in Sweden using a multi-terawatt laser. The scheme of the layout of the experimental chamber is represented in Fig. 1. A titanium-doped sapphire (Ti:Sa) laser delivers pulses with FWHM duration of 40 fs at a wavelength of 800 nm by using chirped pulse amplification (CPA). The laser radial profile is corrected by a deformable mirror before focusing by a $f = 78$ cm off-axis parabola. This produces beams with gaussian-like transverse profile, as seen in Fig. 2(a). The profile of the laser intensity distribution in the focal plane, measured in vacuum with a CCD camera, is represented by the blue crosses. The blue solid line represents the best fit of the experimental points to a gaussian function. As part of the signal in the wings was not detected by the camera, only the central part of the laser intensity distribution was used for the fitting. The laser transverse size $w_0$ at waist, *i.e.* radius at $e^{-2}$, is measured to be about 17 µm (black vertical line). The energy on target is measured to be $E_L = (830 \pm 30)$ mJ and its proportion contained within a circle having a radius equal to $w_0$ is 88%. The laser peak intensity is thus estimated to be $I_{peak} = (3.8 \pm 0.2) \times 10^{18}\,\mathrm{W/cm}^2$ giving a normalized vector potential of $a_0 = eA/m_ec^2 \approx 1.3 - 1.4$. An active system for stabilizing the laser pointing, developed[23] at LLC, was used in this experimental campaign, giving a standard deviation of the laser pointing of ≈ 4 µrad and improving the electron properties as well as extending the lifetime of capillary tubes.[24]

### 2.2 Electron and X-ray Diagnostics

Spectra of accelerated electron bunches were studied using a 12 cm long dipole magnet with a peak field of 0.7 T, located 13 cm after the capillary entrance. After being deflected by the magnet, the electrons drifted 16 cm before impinging on a scintillating screen (Kodak Lanex Regular). The radiation emitted by the lanex was imaged by a 16-bit CCD camera located outside of the vacuum chamber. Both the energy and the divergence spectra of bunches were obtained from the analysis of the distribution of the lanex emission. The lowest energy that could be measured with this setup was about 40 MeV. The charge $Q_e$ was calculated from the image of the scintillating screen using published calibration factors[25] . Finally, the average full width at half maximum (FWHM) divergence ( $\langle\theta_e^{FWHM}\rangle$ ) of the electron bunches was estimated as follows: (i) Both the charge ($dQ_e/dE_e$) and the FWHM

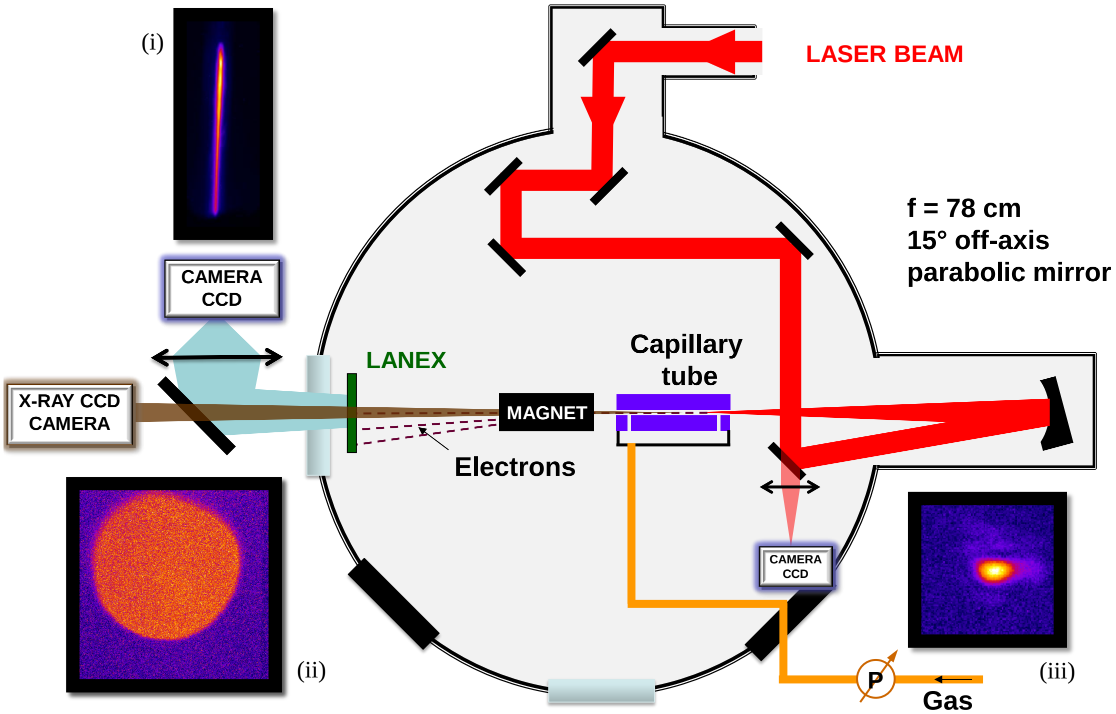

Figure 1. Layout of the experimental chamber implemented for the experimental campaign at the Lund Laser Centre. A multi-terawatt laser system, including a deformable mirror and an active system stabilizing the laser pointing (not represented on this scheme), was employed. (i) Typical radiation emitted by the scintillating screen, *i.e.* electron energy distribution when the magnet is on axis, (ii) typical betatron radiation exiting by the hole of the capillary tube, and (iii) typical laser focal spot are shown. For clarity of the scheme, the electron dispersion is drawn horizontally whereas they were deflected downward during the experiment.

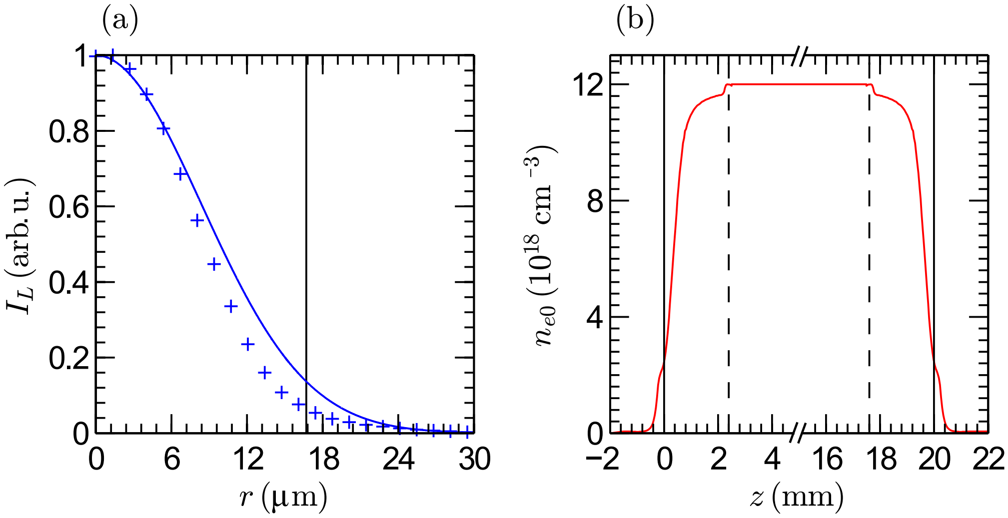

Figure 2. (a) Experimental radial profile (blue crosses) of the laser intensity ($I_L$), in vacuum, at the focal plane. The solid blue line indicates the best fit of the central part of the experimental points with a gaussian function. The vertical black solid line defines the laser size at waist $w_0$. (b) Electron number density (red solid line) as a function of the longitudinal position $z$, within a 20 mm long, 152μm diameter dielectric capillary tube. The locations of the capillary exits and the slits are indicated by the vertical solid and dashed lines, respectively.

divergence ($\theta_e^{FWHM}$) are calculated in term of the electron energy ($E_e$), (ii) the average FWHM divergence is determined using the formula :

$$\langle \theta_e^{FHWM} \rangle = \frac{\int \theta_e^{FWHM}\left(E_e\right) \frac{dQ_e}{dE_e}\, dE_e}{\int \frac{dQ_e}{dE_e}\, dE_e} \tag{1}$$

The X-ray emission was recorded with a 16-bit X-ray CCD camera, its features have been characterized by Fullagar *et al.*[26] . An array of thin metallic filters was positioned in front of the camera in order to estimate the critical energy using the method of Ross' filters, assuming a synchrotron-like spectrum.

### 2.3 Gas Target: Dielectric Capillary Tubes

A glass capillary tube, with length of $L_{cap} = 20\,\mathrm{mm}$, and inner radius $r_{cap} = 73\,\mu\mathrm{m}$, was used to confine and control the gas distribution. It was mounted in a motorized holder allowing its accurate alignment, in vacuum, on the laser axis. The gas used for studying self-injection was pure hydrogen ($H_2$), and two gas mixtures for ionization-induced injection. We name these mixtures as nitrogen ($N_2$) mixture and argon (Ar) mixture, which are composed of $99\%H_2 + 1\%N_2$ and $99\%H_2 + 1\%\mathrm{Ar}$, respectively. The gas was let in through two slits located at 2.5 mm from the tube exits, providing a 15 mm long plateau with constant pressure between the two slits. The molecular density inside the capillary tubes was adjusted by a gas regulator controlling the upstream reservoir pressure. The gas density was calibrated off-line by interferometric studies[27] coupled with fluid simulations using the *sonicfoam* solver of OpenFOAM code[28, 29] . The simulated longitudinal profile of the electron number density is represented in Fig. 2(b); the locations of the capillary exits and the slits are indicated by the black solid and dashed lines, respectively. The electron number density of the plateau, with and without nitrogen or argon, is $n_{e0} = (12 \pm 2) \times 10^{18}\,\mathrm{cm}^{-3}$, assuming complete ionization of the atoms.

## 3. EXPERIMENTAL RESULTS

### 3.1 Electron Acceleration

The energy spectra of electron bunches accelerated in pure $H_2$, nitrogen mixture and argon mixture media are given in Fig. 3(a), (b) and (c), respectively. These data were acquired from a sequence of 30 shots in the case of pure $H_2$ and nitrogen mixture, and a sequence of 8 shots when the argon mixture was employed. The mean spectra are represented by the solid lines whereas the dashed lines illustrate its standard deviation. For these experimental parameters, electron bunches with broad energy spectra were measured, suggesting continuous injection. The resulting detected charge ($Q_e$), with energy above 40 MeV, was estimated to be $55 \pm 10$ pC for pure $H_2$, $100 \pm 20$ pC for the nitrogen mixture, and $130 \pm 40$ pC for the argon mixture. It was found that the average energy is approximately 70 MeV for the three cases, giving a Lorentz factor ($\gamma_e$) of about 140.

Similarly, the divergence spectra of the electron bunches as a function of electron energy is plotted for pure $H_2$, nitrogen mixture and argon mixture media in Fig. 3(d), (e) and (f), respectively. In the case of pure $H_2$, the signal was too low to compute the FWHM divergence for energies higher than 130 MeV. Using Eq. 1, the FWHM divergence is estimated to be $6 \pm 1$ mrad for pure $H_2$, $23 \pm 3$ mrad for nitrogen mixture and $24 \pm 5$ mrad for argon mixture.

### 3.2 X-ray Generation

The characterization of the X-ray beams exiting the capillary tubes provides valuable insight on the electron injection and dynamics during acceleration. On one hand, it allows an estimate of the transverse amplitude of betatron oscillation, which is assumed to be the source size of the emitted X-ray radiation. On the other hand, it is possible to determine the profile of betatron emission which is directly linked to the dynamics of electron acceleration. The X-ray beams generated during the acceleration process are depicted by the typical image of the integrated X-ray beam shown in Fig. 1(ii). As the emission angle of the betatron radiation is much larger ($\sim 100\,\mathrm{mrad}$) than the aperture angle of the capillary tubes ($\sim 10\,\mathrm{mrad}$) in the present case, the X-ray beam will be cropped by the capillary walls. This allows the use of capillary tubes for pinhole imaging as discussed in Sec. 3.2.2. Moreover, published tables[30] indicate that the X-ray beams are not absorbed by the gas.

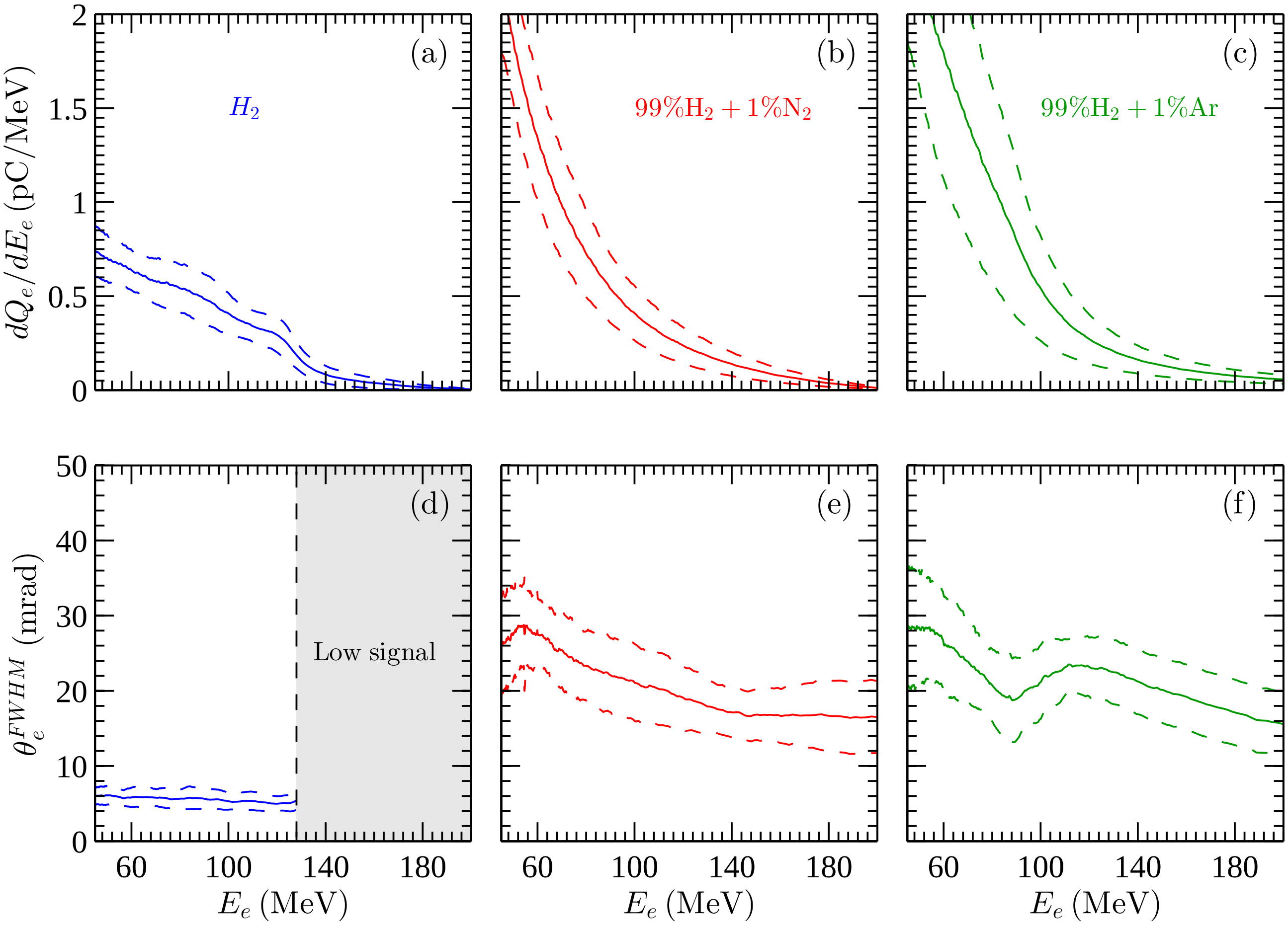

Figure 3. Mean energy spectra (solid curves) of electron bunches for a sequence of 30 shots performed at $n_0 = (12 \pm 2) \times 10^{18}\,\mathrm{cm}^{-3}$ with pure $H_2$ (a) , nitrogen mixture (b) and argon mixture (c). The dashed curves indicate the standard deviation from the mean spectra. (d-f) Corresponding FWHM divergence curves. The gray area shows the energy range where the signal was too low to compute the FWHM divergence.

### 3.2.1 Synchrotron Spectra and Critical Energy

Assuming a synchrotron-like spectrum[13] , the critical energy of an X-ray beam is given[31] in the wiggler regime as

$$E_c = \frac{3\gamma_e^2 r_\beta \hbar\omega_p^2}{2c}, \tag{2}$$

where $r_\beta$ and $\omega_p$ are the source size and the plasma frequency, respectively. $E_c$ was estimated from a least squares method using the transmission data of the filters and the sensitivity of the imaging system[14] . The critical energy was only determined for the pure $H_2$ and nitrogen mixture. It is found to be independent of the type of gas. The average critical energy for all the shots shown in Fig. 3(a) and (b) was computed to be $5.2 \pm 1.0\,\mathrm{keV}$, giving rise to an X-ray source size of $r_\beta \approx 2.2 \pm 0.5\,\mu\mathrm{m}$ (see Eq. 2). We assumed here the betatron radiation from the argon mixture medium to have a critical energy similar to the one measured for pure $H_2$ and nitrogen mixture media.

### 3.2.2 Profiles of X-ray Beams

The X-ray radiating zone along the capillary axis inside the plasma can be determined by analyzing the transverse spatial distribution of the cropped X-ray beam exiting the capillary tubes[21,22] . This method assumes that: (i) X-ray photons are emitted on the capillary axis, (ii) the radiation source is ponctual ($r_\beta \ll r_{cap}$). The radial variation of the X-ray signal ($S_{chip}(r)$) in the detector plane can be transformed into the longitudinal intensity ($I\,(z)$) of the X-ray emission inside the plasma by using the following system of equations :

$$z = L_{cap} - D_X \frac{r_{cap}}{r}, \tag{3}$$

$$I\,(z) = -\frac{\partial S_{chip}(r)}{\partial r} \frac{r^2}{r_{cap} D_X}, \tag{4}$$

where $D_X = 1220\,\mathrm{mm}$ is the distance between the X-ray source and the detector. The azimuthal average of the X-ray signal on the detector (Fig. 4(a)) shows that the peak value of the X-ray fluence for the nitrogen mixture (red solid line) and argon mixture (green dot-dash line) is twice that of pure $H_2$ (blue dashed line). The fluctuations of $S_{chip}$ for $r < 2$ mm is attributed to X-ray reflection. This artefact has been highly mitigated by carefully chosing the region of interest used for plotting the radial profile, in such a way it does not affect the analysis of the betatron emission profiles. The peak fluence for the nitrogen mixture case is estimated to be $\sim 10^5\,\mathrm{ph/mrad^2}$. Kostyukov *et al.* shows[10] that the fluence ($\Gamma_X$) of betatron radiation emitted by an electron bunch oscillating within an ion plasma channel is

$$\Gamma_X = 5.6 \times 10^{-3} \times N_\beta \gamma_e^2 Q_e\,. \tag{5}$$

The number of oscillations can be estimated as $N_\beta = L_\varphi/\lambda_\beta \propto n_0^{-1}\gamma_e^{-1/2}$, where $L_\varphi$ is the dephasing length of electrons and $\lambda_\beta$ the betatron oscillation wavelength. As $\gamma_e$ and $n_0$ are similar for the three cases, the higher fluence observed in the presence of the mixture is pre-dominantly due to an increase of the electron bunch charge. The betatron emission profiles are plotted in Fig. 4(b) and give rise to two main conclusions:

1. Assuming that the start of charge trapping is similar to the onset of betatron emission, Fig. 4(b) shows that the onset of charge trapping occurs earlier with the presence of $N_2$ or Ar than with pure $H_2$. As the electron number density is similar for all the gases, the non-linear evolution of the laser pulse enveloppe during the propagation is similar for the three cases, as confirmed by simulations (Fig. 5(a)).
2. The emission length for both gas mixtures is about 5 mm whereas it is 3 mm for pure $H_2$. For all the gases, the X-ray emission length is significantly larger than the dephasing length which is estimated[32] to be

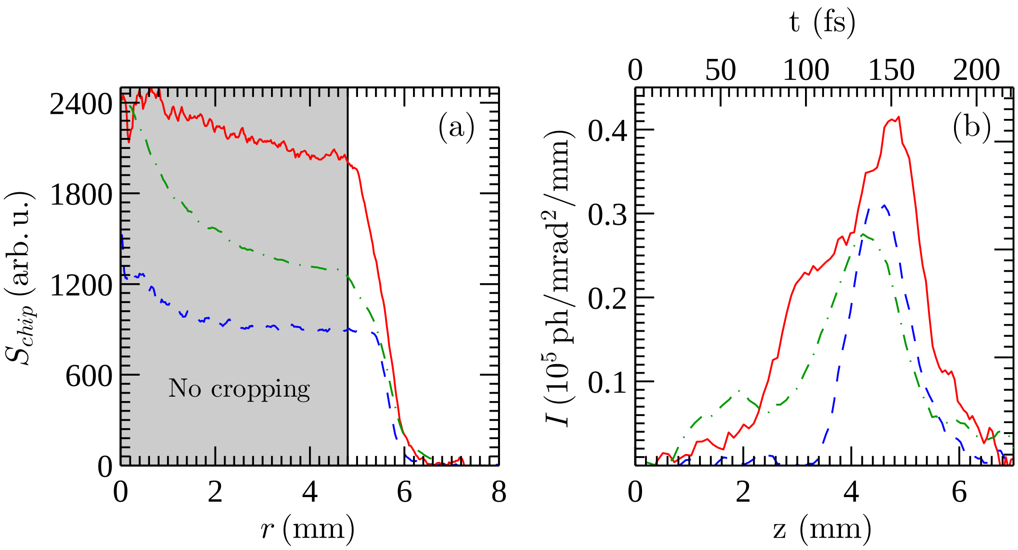

Figure 4. Typical experimental profiles of X-ray beams for pure $H_2$ (blue dashed line), nitrogen mixture (red solid line) and argon mixture (green dot-dash line) at $(11 \pm 1) \times 10^{18}\,\mathrm{cm^{-3}}$: (a) Azimuthal average of the X-ray signal on the detector, and (b) corresponding calculated longitudinal profile of emission. The grey area represents the central part of the X-ray profile that is not cropped by the capillary tube.

> $L_\varphi \simeq 400\,\mu\mathrm{m}$. It indicates a continuous injection of electrons over the emission length. Assuming that the X-ray radiation source moves inside the plasma with the laser group velocity, we can estimate the temporal profile of the X-ray pulse using the transformation $t = z(v_g^{-1} - c^{-1})$ where $v_g$ is the group velocity of the laser pulse. The corresponding time scale is shown on the top horizontal axis in Fig. 4(b).

The analysis of 10 shots shows that, on average, the FWHM of X-ray emission duration is 47 fs for pure $H_2$ and 53 fs for nitrogen mixture media. The corresponding peak brightness for nitrogen mixture case is estimated to be $\sim 5 \times 10^{20}$ photons/(s mm$^2$mrad$^2$0.1%BW) and the number of photons $\sim 10^9$.

## 4. PARTICLE-IN-CELL SIMULATIONS AND DISCUSSION

### 4.1 Simulation Settings

These experimental results are qualitatively analyzed using Particle-In-Cell (PIC) simulations in two dimensional cartesian geometry with the code WARP[33] . Ionization dynamics is described by a field ionization model[34] implemented in WARP. In order to identify the origin of trapped electrons, different electron species are created for each possible ionization state of hydrogen (H), helium (He), nitrogen (N) and argon (Ar). The corresponding ionization potentials (IP) are reported in Tab. 1. The cells are shaded according to the dynamics of the electrons after ionization, as discussed in Sec. 4.2; this is not based on the atomic structure. The cells colored in light gray, white and dark gray refer to, arbitrarily named, low IP (LIP), medium IP (MIP) and high IP (HIP), respectively. In the following discussion on gas mixture, LIP electrons will refer to a group of electrons including hydrogen electrons and those coming from the LIP shells of nitrogen or argon.

The glass capillary tube (dielectric constant = 2.25) is modelled by two dielectric slabs separated by a distance equal to the inner diameter of the capillary tube. As shown by the grey area in Fig. 5(a), the longitudinal profile of plasma density is set to be a linear density ramp near the capillary entrance followed by a plateau of density $n_0 = 11 \times 10^{18}\,\mathrm{cm}^{-3}$. The laser pulse with $a_0 = 1.3$, waist size $w_0 = 17\,\mu\mathrm{m}$ and duration (FWHM) $\tau_L = 40\,\mathrm{fs}$ is focused at $z = 1\,\mathrm{mm}$. The grid resolution in $Z$ and $X$ directions is $0.04\,\mu\mathrm{m}$ and $0.33\,\mu\mathrm{m}$, respectively, with 4 macro-particles per cell.

| H | He | N | Ar |
|---|---|---|---|
| 13.6 | 24.6 | 14.5 | 15.8 |
| | 54.4 | 29.6 | 27.6 |
| | | 47.5 | 40.7 |
| | | 77.5 | 59.8 |
| | | 97.9 | 75.0 |
| | | 552.1 | 91.1 |
| | | 667.0 | 124.3 |
| | | | 143.5 |
| | | | 422.5 |
| | | | 478.7 |
| | | | 539.0 |
| | | | 618.3 |
| | | | 686.1 |
| | | | 755.7 |
| | | | 854.8 |
| | | | 918.0 |
| | | | 4121.0 |
| | | | 4426.0 |

Table 1. Table of ionization potentials in electron-volt for the hydrogen (H), helium (He), nitrogen (N) and argon (Ar). The light gray cells show the low ionization potential (LIP) for which electrons contribute to the plasma wake. No significant amount of these electrons are trapped and accelerated. The white cells contain the medium ionization potential (MIP). MIP electrons are potentially trapped by the plasma wave. The dark gray cells indicate the non-ionized argon shells with a high ionization potential (HIP).

### 4.2

### Parameters of Laser Beam and Electron Bunches

The simulated evolution of the laser $a_0$ and accelerated charge $Q$ (with energy above 40 MeV) along the longitudinal direction $z$ is plotted in Fig. 5 for pure $H_2$ (blue dashed line), nitrogen mixture (red solid lines) and argon mixture (green dot-dash lines). In all cases, self-focusing of the laser pulse causes $a_0$ to increase above the thresholds of self-injection and ionization-induced injection (see Fig. 5(a)). Typically, for our operating conditions, ionization-induced injection is expected[20] to occur for $a_0 \approx 1.7$ whereas self-injection will occur for[32] $a_0 > 2$. The locations $z$ where the laser intensity reaches the thresholds of self-injection and ionization-induced injection are shown by the dashed and solid black lines, respectively. The dynamics of electron injection is discussed for the three cases.

Firstly, we observe on Fig. 5(b) that, for the pure $H_2$ medium, the onset of hydrogen electron trapping is located at $z \approx 2.7\,\mathrm{mm}$. The corresponding intensity of the laser pulse is $a_0 = 3$, well above the theoretical threshold of self-injection.

Secondly, in the case of nitrogen mixture, the amount of trapped

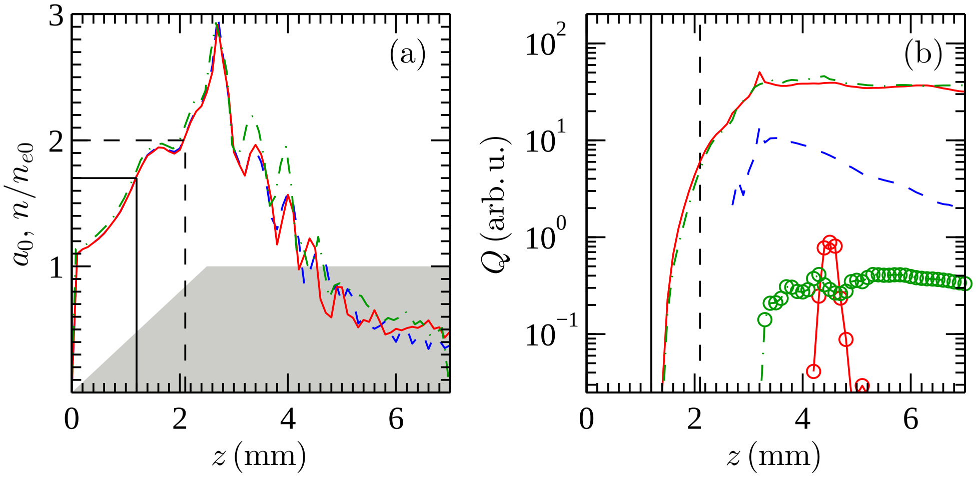

Figure 5. Simulated normalized vector potential $a_0$ of the laser beam and gas profile (grey area) (a), bunch charge (b) as functions of plasma length for pure $H_2$ (blue dashed line), nitrogen mixture (red solid lines) and argon mixture media (green dot-dash lines). The black dashed and solid lines indicate the theoretical thresholds of self-injection and ionization-induced injection, respectively. In case of mixture, the lines with and without circles represent the trapped charge coming from LIP and MIP, respectively.

LIP and MIP electrons are represented in Fig. 5(b) by a red solid line with and without circles, respectively. It shows that the amount of MIP electrons is two orders of magnitude higher than that of accelerated electrons with a LIP, which confirms that more electrons are trapped when nitrogen mixture is employed (see Fig. 3(a),(b)). As electron injection starts at $z \approx 1.4\,\mathrm{mm}$, a position where laser intensity ($a_0 \approx 1.8$) is below the self-injection threshold, it shows that the injection of MIP electrons can only be attributed to ionization-induced injection. However, as soon as the laser intensity is above the self-injection threshold ($z > 2.1\,\mathrm{mm}$), the two mechanisms are possibly in competition. Previous work[35] showed that, in the case of nitrogen mixture, self-injection of LIP electrons is suppressed by the ionization-induced injection of MIP electrons. The LIP electrons coming transversely to the axis are repelled by the presence of longitudinally injected MIP electrons near the axis. This suppression is possible because, for our experimental conditions, the evolution of $a_0$ is such that the onsets of self-injection and ionization-induced injection are clearly separated in space and time, as it can be seen by comparing the two vertical lines in Fig. 5(a). The threshold for ionization-induced injection is reached before the trapping of self-injected electrons could take place. It was found that ionization-induced injection starts at $\sim 1$ mm before self-injection (Fig. 5(b)) which is consistent with the experimental results (see Fig. 4(b)). The continuous injection of MIP electrons is possible over a longer distance than the dephasing length, it results in the increase of radiating charge in ionization-induced injection compared to the self-injection process.

Thirdly, a trend similar to the nitrogen case is observed when the argon mixture is employed. The amount of trapped LIP and MIP electrons is plotted in Fig. 5(b) by a green solid line with and without circles, respectively. We note that the intensity of the laser pulse did not reach a peak value high enough[36] ($a_0 > 20$ for $\tau_L = 40\,\mathrm{fs}$) to ionize the argon HIP electrons. As suggested by the experimental results on X-ray emission (Fig. 4), the simulation shows that the amount of trapped charge, as well as the dynamics of electron injection, is similar to the nitrogen case. This observation may differ at higher laser intensity. McGuffey *et al.* reported a different electron injection dynamics for a $a_0 = 4$ and $n_{e0} = 10^{19}\,\mathrm{cm}^{-3}$ in a $95\%\mathrm{He} + 5\%\mathrm{N}_2$ medium: LIP and MIP electrons were indifferently and transversely injected. This is infered to result from an ionization of MIP electrons located at the front of the laser pulse where the residual transverse momentum given to them is high. As argon MIP electrons have a different IP range compared to nitrogen MIP electrons (Tab. 1), this change in electron injection scheme may occur at a different laser intensity for argon mixture. Dynamics of argon electron injection will be the topic of future investigations.

## 5. CONCLUSION

Through an experimental study of betatron radiation, as well as two dimensional PIC simulations, we demonstrate the early onset of ionization-induced injection in a LWFA regime in which both ionization-induced injection and self-injection are possible. We find that a higher X-ray fluence ($\sim 10^5\,\mathrm{ph/mrad^2}$) is achieved in the case of ionization-induced injection compared to the case of self-injection. This is inferred to be the consequence of the increased amount of trapped charge observed in presence of ionization-induced injection, resulting from a longer injection length due to a lower injection threshold. Finally, we observe that the early onset of ionization-induced injection suppresses the transverse self-injection process in the regime where both self-injection and ionization-induced injection can occur.

## ACKNOWLEDGMENTS

This project has benefited from financial support from the Triangle de la Physique, the Labex PALM, ARC, the Swedish Research Council, the Knut and Alice Wallenberg Foundation, the Swedish Foundation for Strategic Research, the Lund University X-ray Centre (LUXC), Laserlab-Europe/CHARPAC (Grant agreement 284464, EC's 7th Framework Programme), EuCARD2/ANAC2 (Grant agreement 312453, ECs 7th Framework Programme) and US-DOE (Contracts DE-AC02-05CH11231). J. Ju acknowledges financial support from the Chinese Scholarship Council (CSC).

## REFERENCES

[1] T. Tajima and J. M. Dawson, "Laser electron accelerator," *Phys. Rev. Lett.* **43**, pp. 267–270, Jul. 1979.

[2] A. Modena, Z. Najmudin, A. Dangor, C. Clayton, K. A. Marsh, C. Joshi, V. Malka, C. Darrow, C. Danson, D. Neely, and F. Walsh, "Electron acceleration from the breaking of relativistic plasma waves," *Nature* **377**, pp. 606–608, Oct. 1995.

[3] K. Nakajima, D. Fisher, T. Kawakubo, H. Nakanishi, A. Ogata, Y. Kato, Y. Kitagawa, R. Kodama, K. Mima, H. Shiraga, K. Suzuki, K. Yamakawa, T. Zhang, Y. Sakawa, T. Shoji, Y. Nishida, N. Yugami, M. Downer, and T. Tajima, "Observation of ultrahigh gradient electron acceleration by a self-modulated intense short laser pulse," *Phys. Rev. Lett.* **74**, pp. 4428–4431, May 1995.

[4] D. Umstadter, S.-Y. Chen, A. Maksimchuk, G. Mourou, and R. Wagner, "Nonlinear optics in relativistic plasmas and laser wake field acceleration of electrons," *Science* **273**, pp. 472–475, Jul. 1996.

[5] J. Faure, Y. Glinec, A. Pukhov, S. Kiselev, S. Gordienko, E. Lefebvre, J.-P. Rousseau, F. Burgy, and V. Malka, "A laser-plasma accelerator producing monoenergetic electron beams," *Nature* **431**, pp. 541–544, Sept. 2004.

[6] C. G. R. Geddes, C. Toth, J. van Tilborg, E. Esarey, C. B. Schroeder, D. Bruhwiler, C. Nieter, J. Cary, and W. P. Leemans, "High-quality electron beams from a laser wakefield accelerator using plasma-channel guiding," *Nature* **431**, pp. 538–541, Sept. 2004.

[7] S. P. D. Mangles, C. D. Murphy, Z. Najmudin, A. G. R. Thomas, J. L. Collier, A. E. Dangor, E. J. Divall, P. S. Foster, J. G. Gallacher, C. J. Hooker, D. A. Jaroszynski, A. J. Langley, W. B. Mori, P. A. Norreys, F. S. Tsung, R. Viskup, B. R. Walton, and K. Krushelnick, "Monoenergetic beams of relativistic electrons from intense laser-plasma interactions," *Nature* **431**, pp. 535–538, Sept. 2004.

[8] A. Pukhov and J. Meyer-ter Vehn, "Laser wake field acceleration: the highly non-linear broken-wave regime," *Applied Physics B* **74**, pp. 355–361, Apr. 2002.

[9] S. P. D. Mangles, G. Genoud, M. S. Bloom, M. Burza, Z. Najmudin, A. Persson, K. Svensson, A. G. R. Thomas, and C.-G. Wahlström, "Self-injection threshold in self-guided laser wakefield accelerators," *Phys. Rev. ST Accel. Beams* **15**, p. 011302, Jan. 2012.

[10] I. Kostyukov, S. Kiselev, and A. Pukhov, "X-ray generation in an ion channel," *Physics of Plasmas (1994-present)* **10**, pp. 4818–4828, Nov. 2003.

[11] S. Corde, C. Thaury, A. Lifschitz, G. Lambert, K. Ta Phuoc, X. Davoine, R. Lehe, D. Douillet, A. Rousse, and V. Malka, "Observation of longitudinal and transverse self-injections in laser-plasma accelerators," *Nat. Commun.* **4**, p. 1501, Feb. 2013.

[12] A. Rousse, K. T. Phuoc, R. Shah, A. Pukhov, E. Lefebvre, V. Malka, S. Kiselev, F. Burgy, J.-P. Rousseau, D. Umstadter, and D. Hulin, "Production of a kev x-ray beam from synchrotron radiation in relativistic laser-plasma interaction," *Phys. Rev. Lett.* **93**, p. 135005, Sept. 2004.

[13] S. Fourmaux, S. Corde, K. T. Phuoc, P. M. Leguay, S. Payeur, P. Lassonde, S. Gnedyuk, G. Lebrun, C. Fourment, V. Malka, S. Sebban, A. Rousse, and J. C. Kieffer, "Demonstration of the synchrotron-type spectrum of laser-produced betatron radiation," *New J. Phys.* **13**, p. 033017, Mar. 2011.

[14] S. Kneip, S. R. Nagel, C. Bellei, N. Bourgeois, A. E. Dangor, A. Gopal, R. Heathcote, S. P. D. Mangles, J. R. Marqus, A. Maksimchuk, P. M. Nilson, K. T. Phuoc, S. Reed, M. Tzoufras, F. S. Tsung, L. Willingale, W. B. Mori, A. Rousse, K. Krushelnick, and Z. Najmudin, "Observation of synchrotron radiation from electrons accelerated in a petawatt-laser-generated plasma cavity," *Phys. Rev. Lett.* **100**, p. 105006, Mar. 2008.

[15] J. Ju, K. Svensson, H. Ferrari, A. Dopp, G. Genoud, F. Wojda, M. Burza, A. Persson, O. Lundh, C.-G. Wahlström, and B. Cros, "Study of electron acceleration and x-ray radiation as a function of plasma density in capillary-guided laser wakefield accelerators," *Phys. Plasmas* **20**, p. 083106, Aug. 2013.

[16] M. Chen, Z.-M. Sheng, Y.-Y. Ma, and J. Zhang, "Electron injection and trapping in a laser wakefield by field ionization to high-charge states of gases," *J. Appl. Phys.* **99**, p. 056109, Mar. 2006.

[17] C. McGuffey, A. G. R. Thomas, W. Schumaker, T. Matsuoka, V. Chvykov, F. J. Dollar, G. Kalintchenko, V. Yanovsky, A. Maksimchuk, K. Krushelnick, V. Y. Bychenkov, I. V. Glazyrin, and A. V. Karpeev, "Ionization induced trapping in a laser wakefield accelerator," *Phys. Rev. Lett.* **104**, p. 025004, Jan. 2010.

[18] C. E. Clayton, J. E. Ralph, F. Albert, R. A. Fonseca, S. H. Glenzer, C. Joshi, W. Lu, K. A. Marsh, S. F. Martins, W. B. Mori, A. Pak, F. S. Tsung, B. B. Pollock, J. S. Ross, L. O. Silva, and D. H. Froula, "Self-guided laser wakefield acceleration beyond 1 gev using ionization-induced injection," *Phys. Rev. Lett.* **105**, p. 105003, Sept. 2010.

[19] A. Pak, K. A. Marsh, S. F. Martins, W. Lu, W. B. Mori, and C. Joshi, "Injection and trapping of tunnel-ionized electrons into laser-produced wakes," *Phys. Rev. Lett.* **104**, p. 025003, Jan. 2010.

[20] M. Chen, E. Esarey, C. B. Schroeder, C. G. R. Geddes, and W. P. Leemans, "Theory of ionization-induced trapping in laser-plasma accelerators," *Phys. Plasmas* **19**, p. 033101, Mar. 2012.

[21] G. Genoud, K. Cassou, F. Wojda, H. Ferrari, C. Kamperidis, M. Burza, A. Persson, J. Uhlig, S. Kneip, S. Mangles, A. Lifschitz, B. Cros, and Wahlström, C.-G., "Laser-plasma electron acceleration in dielectric capillary tubes," *Applied Physics B* **105**, pp. 309–316, Apr. 2011.

[22] S. Corde, K. T. Phuoc, R. Fitour, J. Faure, A. Tafzi, J. P. Goddet, V. Malka, and A. Rousse, "Controlled betatron x-ray radiation from tunable optically injected electrons," *Phys. Rev. Lett.* **107**, p. 255003, Dec. 2011.

[23] G. Genoud, F. Wojda, M. Burza, A. Persson, and C.-G. Wahlström, "Active control of the pointing of a multi-terawatt laser," *Rev. of Sci. Instrum.* **82**, p. 033102, Mar. 2011.

[24] M. Hansson, L. Senje, A. Persson, O. Lundh, C.-G. Wahlström, G. Desforges, F. J. Ju, L. Audet, T. B. Cros, S. Dobosz Dufrénoy, and P. Monot, "Enhanced stability of laser wakefield acceleration using dielectric capillary tubes," *Phys. Rev. ST Accel. Beams* **17**, p. 031303, Mar. 2014.

[25] A. Buck, K. Zeil, A. Popp, K. Schmid, A. Jochmann, S. D. Kraft, B. Hidding, T. Kudyakov, C. M. S. Sears, L. Veisz, S. Karsch, J. Pawelke, R. Sauerbrey, T. Cowan, F. Krausz, and U. Schramm, "Absolute charge calibration of scintillating screens for relativistic electron detection," *Rev. Sci. Instrum.* **81**, p. 033301, Mar. 2010.

[26] W. Fullagar, J. Uhlig, M. Walczak, S. Canton, and V. Sundstrom, "The use and characterization of a backilluminated charge-coupled device in investigations of pulsed x-ray and radiation sources," *Rev. Sci. Instrum.* **79**, p. 103302, Oct. 2008.

[27] J. Ju and B. Cros, "Characterization of temporal and spatial distribution of hydrogen gas density in capillary tubes for laser-plasma experiments," *J. Appl. Phys.* **112**, p. 113102, Dec. 2012.

[28] H. G. Weller, G. Tabor, H. Jasak, and C. Fureby, "A tensorial approach to computational continuum mechanics using object-oriented techniques," *Computers in physics* **12**, pp. 620–631, Aug. 1998.

[29] "Openfoam documentation, http://www.openfoam.com/," 2014.

[30] B. Henke, E. Gullikson, and J. Davis, "X-ray interactions: Photoabsorption, scattering, transmission, and reflection at e = 50-30,000 ev, z = 1-92," *Atomic Data and Nuclear Data Tables* **54**, pp. 181–342, July 1993.

[31] E. Esarey, B. A. Shadwick, P. Catravas, and W. P. Leemans, "Synchrotron radiation from electron beams in plasma-focusing channels," *Phys. Rev. E* **65**, p. 056505, May 2002.

[32] W. Lu, M. Tzoufras, C. Joshi, F. S. Tsung, W. B. Mori, J. Vieira, R. A. Fonseca, and L. O. Silva, "Generating multi-gev electron bunches using single stage laser wakefield acceleration in a 3d nonlinear regime," *Phys. Rev. ST Accel. Beams* **10**, p. 061301, Jun. 2007.

[33] J.-L. Vay, D. P. Grote, R. H. Cohen, and A. Friedman, "Novel methods in the particle-in-cell accelerator code-framework warp," *Comput. Sci. Disc.* **5**, p. 014019, Dec. 2012.

[34] G. L. Yudin and M. Y. Ivanov, "Nonadiabatic tunnel ionization: Looking inside a laser cycle," *Phys. Rev. A* **64**, p. 013409, Jun. 2001.

[35] F. G. Desforges, B. S. Paradkar, M. Hansson, J. Ju, L. Senje, T. L. Audet, A. Persson, S. Dobosz-Dufrénoy, O. Lundh, G. Maynard, P. Monot, J.-L. Vay, C.-G. Wahlström, and B. Cros, "Dynamics of ionization-induced electron injection in the high density regime of laser wakefield acceleration," *Phys. Plasmas (1994-present)* **21**, p. 120703, Dec. 2014.

[36] L. Keldysh, "Ionization in the field of a strong electromagnetic wave," *Sov. Phys. JETP* **20**, pp. 1307–1314, Nov. 1965.